Dalton Transactions

ROYAL SOCIETY OF CHEMISTRY

PAPER

View Article Online
View Journal | View Issue

Cite this: *Dalton Trans.*, 2023, **52**, 5715

Highly efficient yellow emission and abnormal thermal quenching in Mn^{2+}-doped Rb_4CdCl_6†

Dayu Huang,‡[a,b] Qiuyun Ouyang,‡[b] Youchao Kong,[c] Bo Wang, *[c] Ziyong Cheng,[a] Abdulaziz A. Al Kheraif,[d] Hongzhou Lian*[a] and Jun Lin *[a]

In this paper, Mn^{2+}-doped Rb_4CdCl_6 metal halide single crystals were prepared by a hydrothermal method. The Rb_4CdCl_6:Mn^{2+} metal halide exhibits yellow emission with photoluminescence quantum yields (PLQY) as high as 88%. Due to the thermally induced electron detrapping, Rb_4CdCl_6:Mn^{2+} also displays good anti-thermal quenching (ATQ) behavior with thermal quenching resistance (131% at 220 °C). The increase in the photoionization and the detrapping of the captured electrons from the shallow trap states were appropriately attributed to this exceptional phenomenon based on thermoluminescence (TL) analysis and density functional theory (DFT) calculations. The relationship between the fluorescence intensity ratio (FIR) of the material and temperature change was further explored using the temperature-dependent fluorescence spectrum. It was used as a temperature measuring probe based on absolute sensitivity (S_a) and relative sensitivity (S_b) with the change in temperature. The phosphor-converted white light emitting diodes (pc-WLEDs) were fabricated using a 460 nm blue chip with a yellow phosphor, which has a color rendering index (CRI = 83.5) and a low correlated color temperature (CCT = 3531 K). Because of this, finding new metal halides with ATQ behavior for high-power optoelectronic applications may be made possible by our findings.

Received 13th February 2023,
Accepted 20th March 2023

DOI: 10.1039/d3dt00453h

rsc.li/dalton

1. Introduction

Metal halide perovskite is an excellent photoelectric functional material. Reports on inorganic halide perovskite materials are endless.[1–3] These materials are utilized extensively in a variety of industries, including the manufacture of solar cells, lighting displays, photodetectors, and photocatalysis.[4,5]

Mn^{2+} is one of the most significant transition metal ions with millisecond lifetimes for its visually distinguishable properties of yellow broadband and green narrowband emission. Metal halides often have higher band gaps than Mn^{2+}, making it simple to transfer energy from the host to Mn^{2+} by modifying the host's band gap. Mn^{2+}-based metal halide perovskites have been successfully synthesized.[6–10] These works primarily concentrate on the thorough examination of Mn^{2+} doping to increase the structural stability of metal halide perovskites and their application in light-emitting diodes (LEDs). However, no abnormal behaviors were observed in these studies and the reasons for abnormalities, such as an increase in temperature, enhancement of luminescence intensity, and the energy transfer mechanism after doping Mn^{2+}, were identified. The reasons for these behaviors are still unclear due to technical limitations. Low-temperature and time-resolved spectroscopic studies have shown that the trap state-mediated energy transfer from the 3D $CsPbCl_3$ host to the Mn^{2+} dopant and direct energy transfer from the band-edge state to the dopant occurs at lower temperatures (<60 K) due to the large barrier (314 meV) between the trap state and the Mn^{2+} d state.[11–13] The findings of the Brovelli group demonstrate that the thermally assisted sensitization of Mn^{2+} emission, which is entirely quenched at T = 200 K, is mediated by a two-step process of exciton localization in a shallow metastable state. At T = 60 K, this emission surprisingly reappears, demonstrating that the energy is transmitted straight from the band-edge state.[11] $(CH_3CH_2NH_3)_2PbBr_4$ has a substantial self-trapped exciton (STE) emission and was developed by the Zhang group. The STE emission is completely suppressed as a result of the

[a]*State Key Laboratory of Rare Earth Resource Utilization, Changchun Institute of Applied Chemistry, Chinese Academy of Sciences, Changchun 130022, P. R. China. E-mail: jlin@ciac.ac.cn*
[b]*Key Laboratory of In-Fiber Integrated Optics, Ministry Education of China, and College of Physics and Opotoelectronic Engineering, Harbin Engineering University, Harbin 150001, China*
[c]*Institute of Applied Physics and Materials Engineering, University of Macau, Macao SAR, 999078, P. R. China*
[d]*Dental Health Department, College of Applied Medical Sciences, King Saud University, Riyadh 12372, Saudi Arabia*

†Electronic supplementary information (ESI) available: Computational density functional theory details of Rb_4CdCl_6:Mn^{2+}, SEM images and XPS spectra, absorption spectra, and band structures are included. CCDC 2205344 and 2205343. For ESI and crystallographic data in CIF or other electronic format see DOI: https://doi.org/10.1039/d3dt00453h

‡These authors contributed equally.

efficient capture of excitons by shallow defects created by doping Mn^{2+} into $(CH_3CH_2NH_3)_2PbBr_4$, which results in a 78% Mn^{2+}-doped quantum efficiency.[12] Transient absorption tests have been used by some researchers to confirm that the formation time of self-trapping excitons is approximately several picoseconds.[14,15] Though it is on the same time scale as the energy transfer from excitons to Mn^{2+}, the time needed to trap excitons with shallow defects is much faster.[16] Therefore, the variation in STE emission intensity can reveal the major energy transfer channel. In other words, the energy transfer from thermal excitons to Mn^{2+} is unaffected by trap-mediated energy transfer, but it quenches the emission of STE.

This work involved the synthesis of Rb_4CdCl_6 with anionic STE emission. Although it has been reported that Rb_4CdCl_6 does not emit at room temperature,[17] our experimental findings show a faint luminescence peak at 490 nm. The host's quantum efficiency is less than 1%, but Mn^{2+}-doped Rb_4CdCl_6 has an 88% photoluminescence quantum efficiency. By varying the Mn^{2+} doping amount, it is possible to completely quench STE emission. Thermoluminescence investigations demonstrate that after Mn^{2+} doping, a larger density of trap states can be created in the matrix to further improve Mn^{2+} emission. The crucial function of trap states in improving luminescence intensity against thermal quenching in Mn^{2+}-doped Rb_4CdCl_6 is revealed by these findings. Variable temperature fluorescence spectra were used to further study the relationship between a material's FIR and temperature change, demonstrating the material's potential as a temperature probe.

2. Experimental

2.1 Chemicals

All chemicals were used without further purification: CdO (Cadmium oxide, Aladdin), RbCl (Rubidium Chloride, Aladdin), HCl aqueous solution, *N*,*N*-dimethylformamide (Aladdin), and $(CH_3COO)_2Mn$ (Manganous acetate, Aladdin). All reactions were performed under ambient conditions.

2.2 Synthesis of Rb_4CdCl_6 and Rb_4CdCl_6:$x$$Mn^{2+}$

Rb_4CdCl_6 and Rb_4CdCl_6:$x$$Mn^{2+}$ (x = 0, 0.05, 0.1, 0.2, 0.3) were synthesized by the hydrothermal method. For the Rb_4CdCl_6 host, RbCl (4 mmol) and CdO (1 mmol) were added into a 25 mL Teflon-lined autoclave. Then, 3 mL of HCl aqueous solution was added into the Teflon-lined autoclave followed by the addition of 3 mL of DMF, which was heated at 150 °C for 2 h and then slowly cooled at 2 °C h^{-1} to room temperature. Finally, the obtained single crystal particles were washed twice with ethanol and dried at 80 °C for 1 h in a furnace.

2.3 Material characterizations

The single crystal X-ray diffraction (SCXRD) data were recorded using a Bruker Apex II CCD diffractometer with the X-ray Mo Kα radiation (λ = 0.71073 Å). A suitable single crystal was selected and kept at room temperature during data collection. Data reduction, experimental absorption correction, and cell refinement were obtained with the software package, APEX3. Using Olex2 software, the structure was solved by the ShelXT structural solution program using the Intrinsic Phasing and refined by the ShelXL refinement package using the least-squares minimization. Phase identity was confirmed by X-ray diffraction using a D8 focus diffractometer (Bruker) with Cu-Kα radiation (λ = 1.5405 Å). The diffuse reflectance spectra (DRS) were tested by UV-visible diffuse reflectance spectroscopy UV–2550 PC (Shimadzu Corporation, Japan). Morphological characterization of Rb_4CdCl_6:Mn^{2+} was performed in a scanning electron microscope (FE-SEM, S-4800, Hitachi). TEM was recorded using an FEI Tecnai G2S-Twin with a field-emission gun operating at 200 kV equipped. Photoluminescence (PL) spectra and temperature-dependent (at −180–100 °C) PL spectra were performed on a fluorescence spectrophotometer with a 450 W xenon lamp as the excitation source equipped with a temperature controller (an Edinburgh Instrument FLS-920). Photoluminescence quantum yield (PLQY) values were collected on an absolute PL quantum yield measurement system (Hamamatsu Photonics K.K., C9920-02 Japan). The Raman in the samples was identified by micro-Raman spectroscopy (Jobin Yvon LabRam UV-IR HR-800). For the temperature-dependent Raman measurements, the samples were mounted on a thermal stage (77.873 K, THMSE6300, Linkam Scientific Instruments). An LTTL-3DS measurement was used to record the 2D TL curves at a heating rate of 2 K s^{-1}. Thermogravimetric analyses used a simultaneous thermal analysis (STA 449 F3). The electroluminescence (EL) performance of the fabricated WLED devices was evaluated using a HAAS 2000 photoelectric measuring system (380–1100 nm, EVERFINE, China).

3. Results and discussion

3.1 Crystal structure and optical properties of the Rb_4CdCl_6 host

Rb_4CdCl_6 single crystal was prepared using the hydrothermal method according to the stoichiometric ratio. The experimental section details the precise feeding. Rb_4CdCl_6 was synthesized as a single crystal that crystallized into a monoclinic system ($R\bar{3}c$) based on single-crystal X-ray diffraction. Table 1 lists the detailed structural parameters. According to Fig. 1a, the structural units of Rb_4CdCl_6 are built up of $[CdCl_6]^{4-}$, $[RbCl_6]^{5-}$ octahedron, and $[RbCl_7]^{6-}$ polyhedron, in which Mn^{2+} ions are known to selectively occupy the 6-coordinated Cd^{2+} sites because of their similar valence states and ionic radii ($R_{Cd^{2+}}$ = 0.95 Å and $R_{Mn^{2+}}$ = 0.67 Å). Fig. 1b depicts the pattern of the sample's powder X-ray diffraction (PXRD). The obtained sample possesses good phase purity as shown by the powder diffraction peak's good agreement with the Rb_4CdCl_6 diffraction peak simulated by a single crystal and the absence of other diffraction peaks. The TEM image (Fig. 1c) clearly shows the shape of the corner-like crystals, demonstrating the excellent crystal quality produced by the hydrothermal method. The crystal structure of Rb_4CdCl_6 has a significant

Table 1 Structural data of single crystal Rb_4CdCl_6 and $Rb_4Cd_{0.95}Cl_6$:0.05Mn^{2+}

Structural parameter	Rb_4CdCl_6	Rb_4CdCl_6:0.05Mn^{2+}
a	12.483 Å	12.4538 Å
b	12.483 Å	12.4538 Å
c	15.640 Å	15.6023 Å
Volume	2110.5 Å^3	2095.67 Å^3
Space group	$R\bar{3}c$	$R\bar{3}c$
Z	6	6
h	17	17
k	17	17
l_{max}	22	22
R(reflections)	0.0323	0.0290
wR_2(reflections)	0.0891	0.0881
CCDC	2205344	2205343†

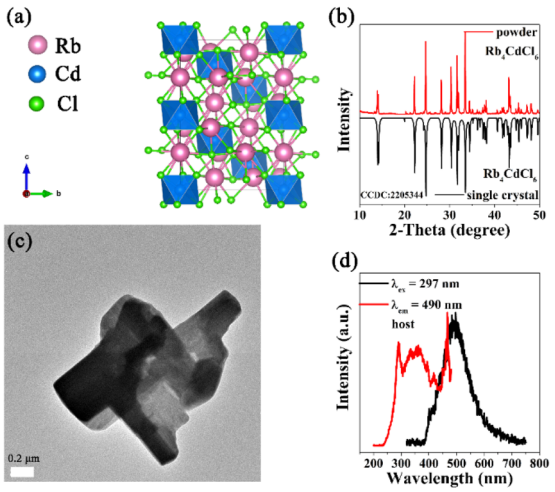

Fig. 1 (a) Crystal structure of Rb_4CdCl_6. (b) PXRD patterns of as-prepared products. (c) TEM image of Rb_4CdCl_6. (d) PL spectrum of Rb_4CdCl_6.

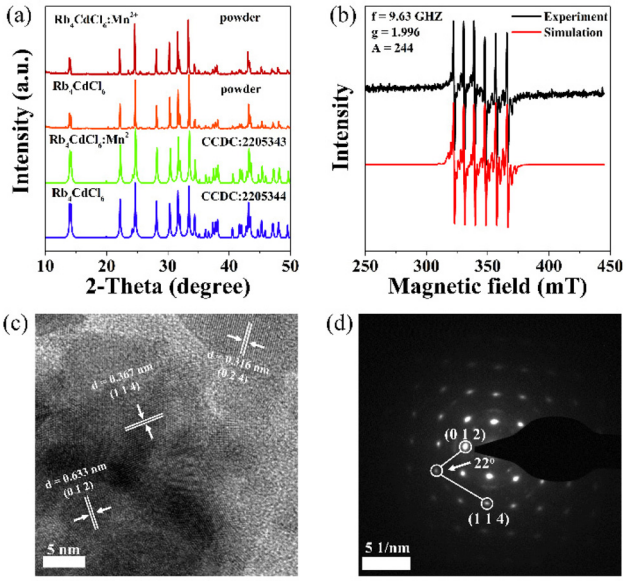

Fig. 2 (a) PXRD patterns of Rb_4CdCl_6 and Rb_4CdCl_6:Mn^{2+}. (b) EPR spectrum of Rb_4CdCl_6:Mn^{2+}. (c) HRTEM image of Rb_4CdCl_6:Mn^{2+}. (d) SAED image of Rb_4CdCl_6:Mn^{2+}.

impact on its optical characteristics. A broad and weak PL band at 490 nm for Rb_4CdCl_6, which is attributed to the anion STE emission, can be observed under 297 nm UV excitation.

3.2 Micro- and electronic structure of Rb_4CdCl_6:Mn^{2+}

The properties of similar structure hosts are also very excellent after Mn^{2+} ions doping, such as high emission quenching temperature and high PLQY.[18] XRD analysis confirmed that both Rb_4CdCl_6 and Rb_4CdCl_6:0.05Mn^{2+} share a similar crystal phase CCDC 2205344† (Fig. 2a). By collecting the single crystal data of Rb_4CdCl_6:Mn^{2+}, we found significant changes in cell parameters (Table 1). The lattice parameters decrease with Mn^{2+} doping, confirming the possibility of replacing Cd sites with Mn^{2+}. Scanning electron microscope images display that Mn^{2+}-doped Rb_4CdCl_6 comprised irregular particles with sizes up to several micrometers (Fig. S1†). Micron-sized crystals with uneven surfaces were observed, indicating that Rb_4CdCl_6 was no longer smooth after Mn^{2+} doping. Mn^{2+} doping introduces a large number of defect energy levels, which may provide a basis for the abnormal thermal stability of luminescent materials. Rb, Cd, Cl, and Mn are equally distributed throughout the crystal samples, according to EDS elemental mapping. The XPS outcomes are displayed in Fig. S2.† Particularly the peak at 653.04 eV corresponds to the binding energy of the 2p of Mn^{2+}, demonstrating the successful introduction of Mn^2; the peaks of Rb, Cd, and Cl are also distinct.

Through XPS, we discovered an intriguing phenomenon in which the signal peaks of Cl in Rb_4CdCl_6 and Cl in Rb_4CdCl_6:Mn^{2+} moved and expanded significantly (Fig. S2e and f†). The material itself has Cl^- vacancy defects; the introduction of Mn^{2+} can control the Cl^- vacancy in a certain range, thereby maintaining high-temperature stability. Due to the high temperature, excessive Cl vacancy defects lead to luminescence quenching. It is further confirmed that Mn^{2+} exists in the material and that just one site in the lattice is suitable for Mn^{2+} as per the EPR spectrum of Mn^{2+} (Fig. 2b) under the influence of an external magnetic field. A weak Mn–Mn dipole contact also exists. Moreover, the results of selected-area electron diffraction (SAED) and high-resolution transmission electron microscopy (HRTEM) for the Rb_4CdCl_6:Mn^{2+} sample are shown in Fig. 2c and d, respectively. Despite the introduction of a large number of defects, there are some places where the crystallinity is good for Rb_4CdCl_6:Mn^{2+} as evidenced by the distinct lattice fringes in the local area of HRTEM and the obvious diffraction sites of SAED. However, many lattice fringe distortions are attributed to defects, and some were broken by electron beams during testing. The crystal plane type and *d*-spacing distances are determined from the diffraction point of SAED and lattice fringes in HRTEM, respectively. Diffraction spots in white circles in the SAED image correspond to the Rb_4CdCl_6's diffraction lattice planes (114) and (012). The theoretical function can determine the angle between the two

crystal planes (114 and 012). The following correlation function can be used to calculate the angle between the two crystal planes.[19]

$$\cos\varphi = \frac{\frac{h_1h_2}{a^2}+\frac{k_1k_2}{b^2}+\frac{l_1l_2}{c^2}}{\sqrt{\left(\frac{h_1^2}{a^2}+\frac{k_1^2}{b^2}+\frac{l_1^2}{c^2}\right)\left(\frac{h_2^2}{a^2}+\frac{k_2^2}{b^2}+\frac{l_2^2}{c^2}\right)}} \quad (1)$$

$a = b = 12.483$ Å, $c = 15.640$ Å. h, k, and l are the indices of crystal planes (114) and (012), respectively. The angle between these two crystal faces is 22°. The three crystal planes that were chosen are indicated in the HRTEM image by the numbers (012), (024), and (114), respectively. The crystal planes have d-spacing values of 0.63, 0.31, and 0.36 nm, respectively.

3.3 Absorption and photoluminescence

Fig. S3a† displays the UV/Vis diffuse reflection (DR) spectrum of Rb_4CdCl_6:Mn^{2+}. The Rb_4CdCl_6:Mn^{2+} exhibited the absorption edge at around 260 nm, corresponding to a bandgap of 4.85 eV. Indeed, the Rb_4CdCl_6:Mn^{2+} exhibited yellow emission to the naked eye under UV irradiation, which is brighter than pristine Rb_4CdCl_6. The room temperature photoluminescence emission (PL) and excitation (PLE) spectra of the Rb_4CdCl_6:Mn^{2+} are recorded. Excitation at 297 nm gives a broadband yellow emission peak at around 580 nm, which is attributed to the spin-forbidden of $^4T_1 \rightarrow {}^6A_1$ transition of Mn^{2+}. According to Fig. 3a, increasing the Mn^{2+} doping concentration can boost PL intensities. After Mn^{2+} doping, the Mn^{2+} d–d emission corresponding to the spin-forbidden $^4T_1 \rightarrow {}^6A_1$ transition can be observed at 580 nm. Unexpectedly, the STE emission is entirely quenched with an increase in the Mn^{2+} dopant concentration. The emission bands of these samples share many solitary excitation bands at 250–325, 325–375, 400, 475, and 550 nm, which may belong to the charge transfer band and electronic transitions from $^6A_{1g}(S)$ to excited state. The corresponding excitation spectrum is shown in Fig. 3b. Distinct transitions are given different excitation peaks. The excitation peak at 250–325 nm belongs to the charge transfer band of the host. The excitation peak at 325–375 nm is attributed to $^4E_g(^4D)/^4T_{2g}(^4D)$-$^6A_1$ transition. The $^4E_{2g}(^4G)/^4T_{2g}(^4G)/^4A_1(^4G)$-$^6A_1$ transition is responsible for the excitation peak between 400 and 475 nm. Moreover, the $^4T_1(^4G)$-$^6A_1$ transition is involved in the excitation peak at 475–550 nm. The samples with the various concentrations had an optimal PLQY at 88% before their sharp decline.

The concentration quenching effect was thought to be responsible for a similar trend to the emission spectra intensity. Fig. 3c and d presents the luminescence photos of the samples under visible and ultraviolet light. The size of the sample and the yellow emission of the sample are also presented. In addition, the single crystal grinding into powder does not affect the luminescence intensity of the sample.

3.4 The abnormal temperature-dependent emission

Intriguingly, Rb_4CdCl_6:Mn^{2+} exhibits excellent anti-thermal-quenching behavior. With the temperature increase from −180 to 260 °C, the emission intensity at first increases, reaches the maximum at 220 °C, and then begins to decrease (Fig. 4a and b). In order to ensure the accuracy and repeatability of the experiment, we tested it repeatedly and the related samples with various content also display similar abnormal-thermal performance. Hence, it may be determined that the anti-thermal quenching phenomenon is derived from the as-synthesized samples. Since significant STE emission can be

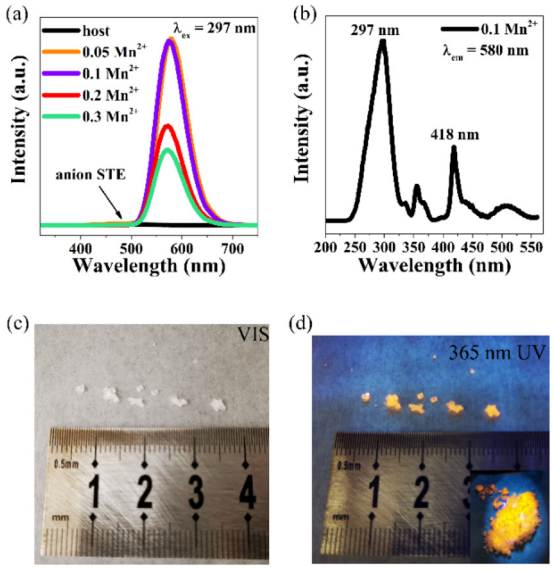

Fig. 3 (a) PL spectra of Rb_4CdCl_6:xMn^{2+}. (b) PLE spectrum of Rb_4CdCl_6:0.1Mn^{2+}. (c and d) Photographs of single crystal Rb_4CdCl_6:Mn^{2+} samples in visible and ultraviolet light, and the insert is a luminescence photograph of the Rb_4CdCl_6:Mn^{2+} powder.

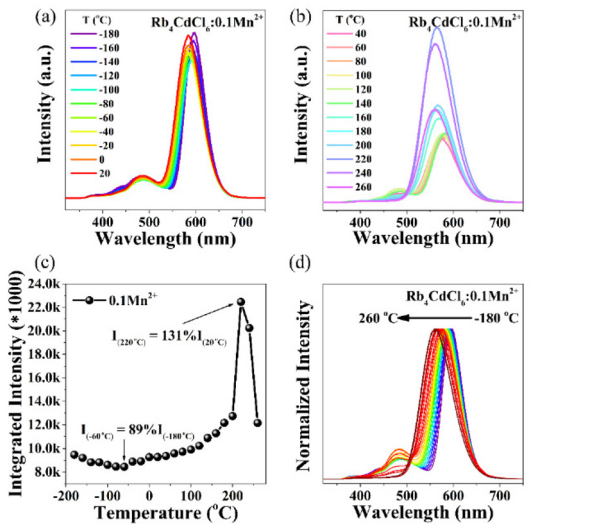

Fig. 4 (a and b) Temperature-dependent PL spectra of Rb_4CdCl_6:0.1Mn^{2+}. (c) The integrated intensity of Rb_4CdCl_6:0.1Mn^{2+} at different temperatures. (d) Normalized intensity of Rb_4CdCl_6:0.1Mn^{2+} at different temperatures.

observed at low temperatures, the whole temperature-rise process referred to multiple photophysical behaviors. First, we observed the normal emission intensity of the Rb_4CdCl_6:Mn^{2+} in region I (−180 to −60 °C) as shown in Fig. 4c. This is originally used to return to the ground state radiation transition energy due to the phonon vibration loss, that is, thermal quenching behavior. Defect levels are not involved in this low-temperature process due to the lack of effective thermal activation energy. In part II (−40–260 °C), the emission intensity at 220 °C remains at 131% of that at 20 °C. Nonetheless, Rb_4CdCl_6:Mn^{2+} exhibits a zero-thermal quenching phenomenon at close to the LED chip working temperature, implying its usefulness for practical purposes. Generally, the electron–phonon coupling becomes stronger and leads to the loss of the luminous intensity under high temperatures.

Hence, the thermal quenching and thermo-stimulated radiation dynamic process may form a competitive relationship to affect the luminescence intensity. Our initial hypothesis was that the STE energy of the host was transferred to Mn^{2+}, however since the STE luminescence is very faint, it is difficult to double the luminescence of Mn^{2+}. Based on the DFT and XPS analysis, the Cl defect level in Rb_4CdCl_6:Mn^{2+} may trap the number of electrons. So we assume a schematic of energy transfer between STE, defects, and Mn^{2+}. When the temperature is lower than 120 °C, the defect state energy level will play an intermediate mediating role, and the energy captured by the defect is transmitted to STE and Mn^{2+}, respectively. At high temperatures, an energy transfer path from STE to Mn^{2+} is added, and then STE is finally quenched. The defect energy level and STE's two-fold energy transfer cause a significant increase in the emission peak of Mn^{2+}. With the increase in temperature, the peak of Mn^{2+} is blue-shifted, and the full width at half maximum (FWHM) is gradually widened (Fig. 4d). The blue shift of the emission peak at high temperatures is because the crystal field strength of the material becomes weaker, which is generally accepted. The emission peak broadening is mainly due to electron–phonon coupling. In addition, we obtained the Debye temperature of Mn^{2+} doping and host by DFT (Fig. S3c†). The structural rigidity and lattice vibration, which may be determined using the following equations, can be estimated using the Debye temperature (θ_D):

$$\theta_D = \frac{h}{k_B}\left[6\pi^2 V^{1/2} N\right]^{1/3}\sqrt{\frac{B_H}{M}} f(\nu) \quad (2)$$

$$f(\nu) = \left\{\left[2\left(\frac{2}{3}\times\frac{1+\nu}{1-2\nu}\right)^{3/2} + \left(\frac{1}{3}\times\frac{1+\nu}{1-\nu}\right)^{3/2}\right]^{-1}\right\}^{1/3} \quad (3)$$

where V is the volume of the unit cell, N is the number of atoms per unit cell, and h is the Planck constant. k_B is the Boltzmann constant. B_H stands for the crystal's adiabatic bulk modulus, M for the molecular mass, and ν for the Poisson ratio. According to DFT calculations, the θ_D for Rb_4CdCl_6 and Rb_4CdCl_6:Mn^{2+} is 179 and 169.5 K, respectively. As compared to the oxide, this value is not very high. This value means that the lattice structure has good rigidity, and the material is not prone to phase transition at high temperatures.

To test the hypothesis proposed above, we include the following data on a series of high-temperature material characterizations. The material's luminous phase did not change at high temperatures, according to high-temperature XRD (Fig. 5a). The temperature-dependent Raman spectra of Rb_4CdCl_6:Mn^{2+} show the same symmetric vibrations (Fig. 5b), indicating that the crystal structure is not affected by the high-temperature treatment. Subsequently, we examined the material's PLQY at different temperatures and discovered that, in addition to the PLQY of the material increasing at high temperatures, the absorption also increased before the maximum and then eventually declined (Table 2). The trend of temperature-dependent quantum efficiency is similar to that of temperature-dependent luminescence. With the increase in temperature, the luminescence of the material is enhanced. It is further proved that the luminescence of the material is indeed enhanced at high temperatures, which is very beneficial for the practical application of the material.

In the information that follows, we demonstrate that the evidence points to the presence of several traps. First, the surface of particles presents the lattice disorder with a certain depth, probably due to the substitution by Mn^{2+} ions (Fig. 6a). Hence, the above finding indicated that the Cl vacancies as

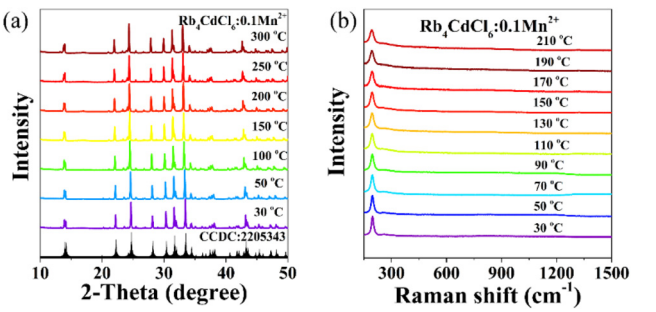

Fig. 5 (a and b) Temperature-dependent XRD and Raman spectra for Rb_4CdCl_6:0.1Mn^{2+}.

Table 2 Dependent temperature PLQY and absorption of Rb_4CdCl_6:Mn^{2+}

Temperature (°C)	Quantum yield	Absorption
25	0.88	0.36
40	0.89	0.37
55	0.90	0.38
70	0.90	0.385
85	0.91	0.389
100	0.92	0.391
115	0.93	0.393
130	0.94	0.396
145	0.95	0.398
160	0.95	0.41
175	0.94	0.412
190	0.94	0.43
205	0.96	0.40
220	0.92	0.402

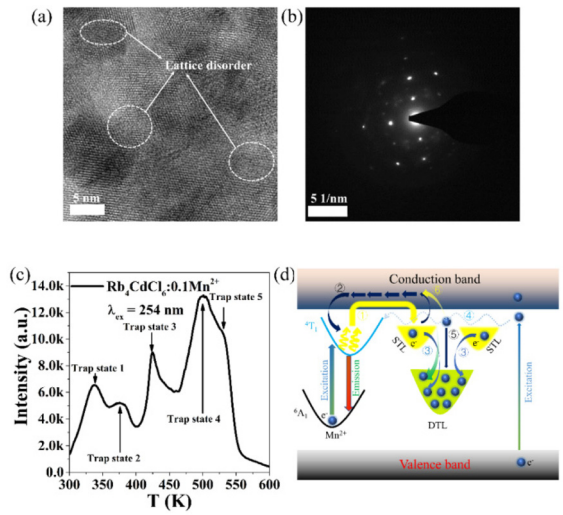

Fig. 6 (a) High-resolution TEM image of Rb_4CdCl_6:0.1Mn^{2+}, the lattice disorder induced by defects is marked by white arrows. (b) SAED image of Rb_4CdCl_6:0.1Mn^{2+}. (c) The thermoluminescence curve. (d) Configurational coordinate diagram. STL: Shallow trap level. DTL: Deep trap level.

electron trapping and storing sites contributed to the enhanced emission intensity. When there is a lot of lattice disorder, the diffraction spots do not match the crystal plane (Fig. 6b). The diffraction point is obviously different from that of a smooth crystal surface (Fig. 2d). To further support this view, the thermoluminescence (TL) glow curve, a powerful tool to investigate the trapping state, was employed. Five trap levels are located between 300 and 600 K at various depths (Fig. 6c). $E = T_m/500$, where E is the average trap depth and T_m is the temperature corresponding to the peak position, is the empirical formula presented by Urbach.[20] The computed trap depths are 0.67, 0.74, 0.85, 1, and 1.062 eV, respectively. Fig. 6d shows several processes of electron transfer. Part of the excited electrons transfer to the excited state of Mn^{2+} at room temperature, enhancing Mn^{2+} emission. Deep traps catch some of them. Additionally, the shallow trap's electron component contributes to the Mn^{2+} emission, and thus boosts it. Deep traps capture the electrons that are left. Deep trap electrons have a key role in the emission of Mn^{2+} at high temperatures. The abnormal luminescence phenomena are caused by the electrons of deep traps obtaining energy to jump out of the deep trap and transfer to the excited state of Mn^{2+}. A host like that is unusual.

3.5 DFT calculations and anti-thermal quenching mechanism

DFT calculations are a powerful method to reveal the structural, electronic, and optical properties of the Rb_4CdCl_6 host and Rb_4CdCl_6:Mn^{2+}. Based on experimental observations, it is reasonable to consider the substitution of Cd^{2+} sites with Mn^{2+} in order to maintain charge balance. The calculated formation of the doped structure is quite small (~0.01 eV, ratio: 20%), which is consistent with the low-temperature fabrication process. Then, the local crystal field will change from $[CdCl_6]^{4-}$ to $[MnCl_6]^{4-}$, showing some characteristics that are different from the host.

Firstly, the introduction of Mn leads to structural distortions in the form of tiny uneven surfaces (Fig. 1c and 2c) and calculated bond length shortening (d_{Rb-Cl}: 3.4 Å; d_{Mn-Cl}: 2.6 Å). Conforming to the Jahn–Teller effect, slight distortions lead to easier STE formation due to the enhanced electron–phonon coupling (Fig. 6a). Secondly, the doping of Mn^{2+} introduces a large number of defect energy states (Fig. 2c), which is a basis for the enhanced STE phenomenon compared to the host. The calculated band gap is shown in Fig. 7a and Fig. S3c.† The band gap is 3.95 eV for Rb_4CdCl_6 and 2.60 eV for Rb_4CdCl_6:Mn^{2+}. The introduction of Mn^{2+} narrows the band gap, which is comparable to the absorption peak appearing in the low-energy region (Fig. S3a† and Fig. 3a).

The DOS of Rb_4CdCl_6 shows that the valence band maximum (VBM) is occupied by the Mn-d and Cl-p orbitals, while the conduction band minimum (CBM) is occupied by the Cd/Rb-d and Cl-p orbitals. In addition, a clear defect trap state is observed near the Fermi level at VBM. In addition, the calculated Debye temperatures for Rb_4CdCl_6 and Rb_4CdCl_6:Mn^{2+} are 179.0 K and 169.5 K. The lower Debye temperatures indicate that the structural lattice tends to soften due to the doping of Mn^{2+}. Herein, the structural distortion and the low Debye temperature prove the properties of STE. Finally, the

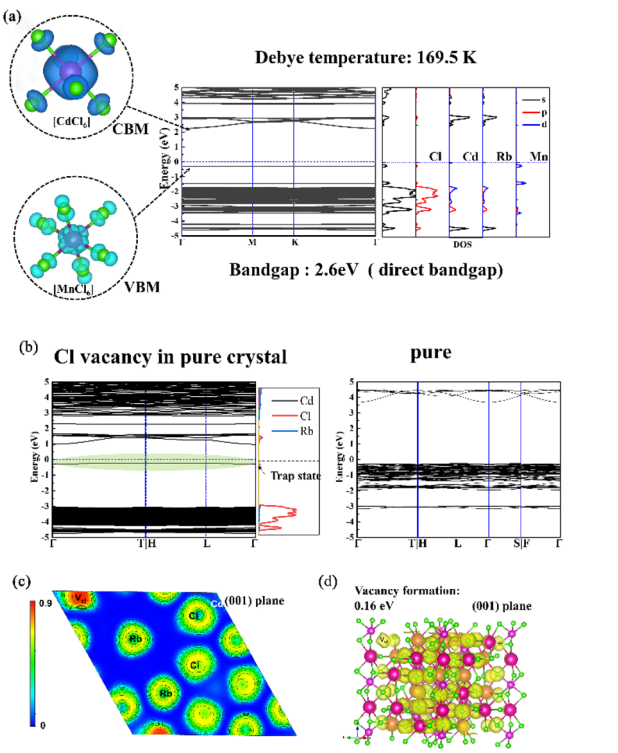

Fig. 7 (a) Debye temperature and calculated electronic structure for Rb_4CdCl_6:Mn^{2+}. (b) Cl vacancy of electronic structure in pure crystal. (c) The distribution of Cl vacancies on the 001 crystal plane. (d) The formation energy of Cl vacancy on 001 crystal plane.

role of Cl vacancies is also worth discussing in detail. In Fig. 7a and b, we find that Cl plays an important role in the electronic structure. XPS shows a certain amount of Cl vacancies in Rb_4CdCl_6 (Fig. S2e and f†). DFT calculations show that Cl vacancies are formed with a small barrier of 0.16 eV (ratio, ~3%), which would lead to a great possibility of Cl vacancies in Rb_4CdCl_6.

Meanwhile, the Cl vacancy brings about a trap state (Fig. 7b–d), which is thought to be a cause of STE in the host. Meanwhile, the ICOHP values of 0.33 and 0.01 eV for Mn–Cl and Rb–Cl, respectively, indicate that the type of bond has changed from ionic to covalent. Therefore, the introduction of Mn prevents the formation of a large number of Cl vacancies at high temperatures and maintains a relatively balanced Cl vacancy ratio, which significantly enhances the anti-thermal quenching of STE. This is because a large number of Cl defects will bring about a large number of nonradiative complexes. This is the reason why we observe the anti-thermal quenching effect at high temperatures.

The trap states of Mn^{2+} materials were computed using a DFT-PBE hybrid functional; the Cl vacancies in the lattice were taken into account (Fig. 7b–d), to further demonstrate that defects are involved in the process of anti-thermal quenching. The energy supplement process: the light irradiation at room temperature/high temperature makes these suitable defect states capture the excited carriers. When the temperature increases, under the action of thermal disturbance, the carriers captured by the defect state are released to the luminescence center, thus making up for the energy loss caused by the thermal quenching effect and improving the thermal stability of the fluorescent material.

We further demonstrated the process of energy transfer from STE to Mn^{2+} by monitoring the decay time of different emission peaks at different temperatures (Fig. 8). By monitoring the excitation and emission spectra of Rb_4CdCl_6 and Mn^{2+} at different temperatures, it is proved that there is energy transfer between Rb_4CdCl_6 and Mn^{2+} at different temperatures. In addition, the decay time test further proves the energy transfer efficiency of the Rb_4CdCl_6 and Mn^{2+}. The conclusion that all data could be explained by a double exponential decay model, $y = y_0 + A_1\exp(-t/\tau_1) + A_2\exp(-t/\tau_2)$, suggests that Rb_4CdCl_6:Mn^{2+} phosphors only contain a double light center. The lifetime of Mn^{2+} increases with increasing temperature, which is strongly related to the material's deep traps. Partly as a result of energy transfer, the host's lifetime keeps getting shorter.

3.6 Application in optical thermal sensing and WLEDs

In optical thermometry, measuring emission intensity using the integral intensity of a single transition or a pair of transitions is the primary approach for determining temperature. The emission intensity of Rb_4CdCl_6 steadily increases with rising temperature (40–260 °C) as shown in Fig. 4.

In contrast to the host emission intensity, the Mn^{2+} emission peak in the Rb_4CdCl_6 matrix increases quickly. Only 20% of the host's emission intensity is present at 20 °C, while the measuring temperature is 220 °C. When the measured temperature reaches 220 °C, the emission intensity of Mn^{2+} is only about 131% of that at 20 °C. As a result, the host's emission intensity can be used as a thermometry probe signal to detect changes in the environmental temperature for phosphors. Additionally, Mn^{2+} emission intensity could be used as a reference signal. Hence, Rb_4CdCl_6:Mn^{2+} phosphor is a material used as a fluorescence thermometer for applications involving temperature sensing.

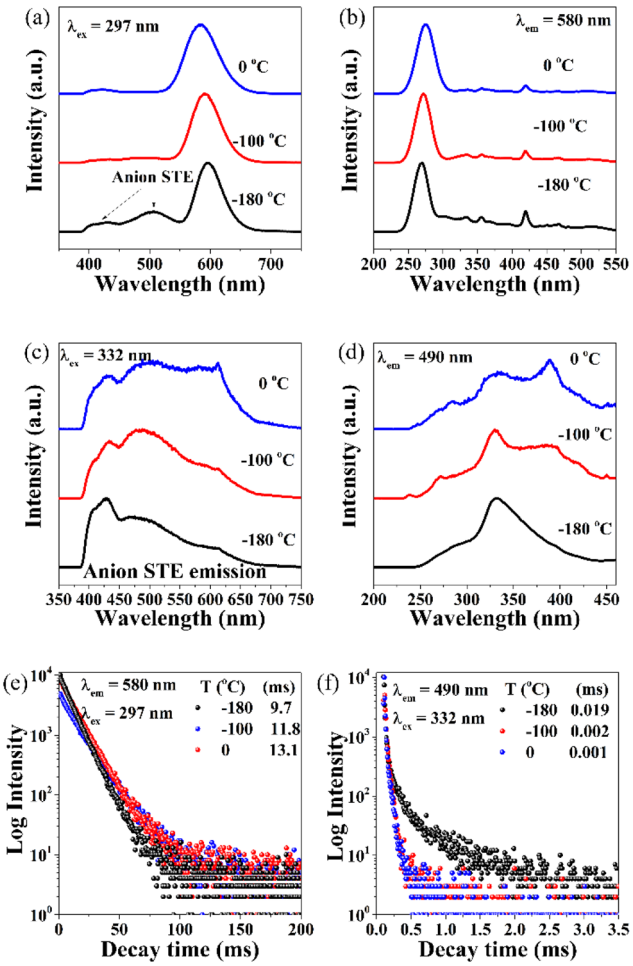

Fig. 8 (a and b) Temperature-dependent PL and PLE spectra of Mn^{2+} in Rb_4CdCl_6:Mn^{2+}. (c and d) Temperature-dependent PL and PLE spectra of the host in Rb_4CdCl_6:Mn^{2+}. (e and f) Temperature-dependent decay curves of Mn^{2+} and host.

The quantitative link between temperature and PL intensity is investigated in order to further examine the suitability of the Rb_4CdCl_6:Mn^{2+} phosphor for temperature monitoring. The link between temperature and the fluorescence intensity ratio (FIR) (I_{Mn}/I_{host}) can be calculated by[21,22]

$$\mathrm{FIR} = A\exp\left(\frac{B}{T}\right) + C \quad (4)$$

T is the temperature in absolute units. The parameters A, B, and C are all related to it. The experimental results are in

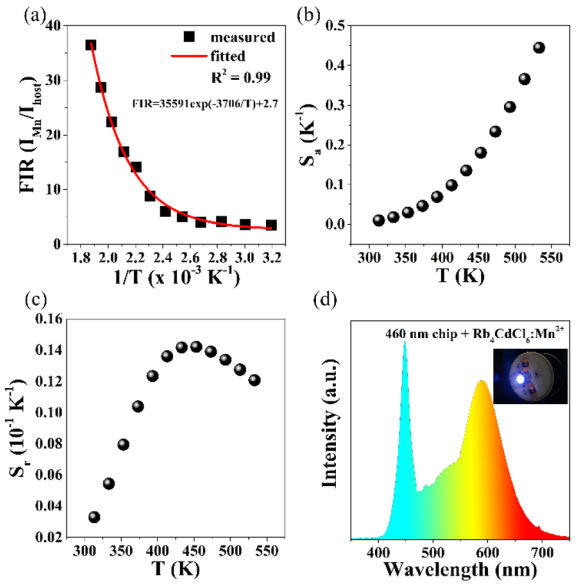

Fig. 9 (a) The fluorescence intensity ratio values temperature. (b and c) The corresponding variation of absolute sensitivity and relative sensitivity. (d) PL spectrum of the white LED fabricated and the inset shows the white light emission from the device operated at 3.0 V.

good agreement with eqn (5) (Fig. 9a). The results are as follows:[21,22]

$$\mathrm{FIR} = 35591 \exp\left(\frac{-3706}{T}\right) + 2.7 \tag{5}$$

$$S_a = \frac{\mathrm{dFIR}}{\mathrm{d}T} = -\frac{AB}{T^2}\exp\left(\frac{B}{T}\right)$$

$$S_r = \frac{1}{\mathrm{FIR}}\frac{\mathrm{dFIR}}{\mathrm{d}T} \times 100\% = \frac{-\frac{AB}{T^2}\exp\left(\frac{B}{T}\right)}{A\exp\left(\frac{B}{T}\right) + C} \times 100\% \tag{6}$$

Two other crucial factors for FIR temperature probes are the absolute sensitivity S_a and the relative sensitivity S_r, which are defined as follows. Fig. 9b and 9c, respectively, depict the change curves for S_a and S_r with temperature. S_r first rises with increasing temperature before decreasing. According to the calculations, the highest values of S_a and S_r are 0.4443 K^{-1} (533.15 K) and 0.0142 K^{-1} (453.15 K), respectively. It demonstrates that the Rb_4CdCl_6:Mn^{2+} material is a reliable FIR temperature probe and has good temperature measurement sensitivity in the high-temperature range.

The performance results of the fabricated pc-WLEDs and associated luminescence images are displayed in Fig. 9d to demonstrate the good luminescence performance of the phosphors. 460 nm blue InGaN chip (3 V, 20 mA) and yellow Rb_4CdCl_6:Mn^{2+} phosphor were combined to create the WLED. The pc-WLED device displays white emission in the test integrating sphere with a low corresponding color temperature (CCT = 3531 K) and a high CRI (R_a = 83.5). The Commission International de l'Eclairage (CIE) chromaticity coordinates of this device are (0.37, 0.31) and its luminous efficiency is 49 lm W^{-1}.

4. Conclusions

The hydrothermal approach proved successful in producing a large single crystal of Mn^{2+}-doped Rb_4CdCl_6. Both the self-trapped exciton emission of the matrix and the yellow emission of Mn^{2+} exhibit bimodal emission characteristics in the crystal. Unexpectedly, Rb_4CdCl_6:Mn^{2+} displayed anti-thermal quenching behavior. This is mostly related to the provision of extra charge carriers to Mn^{2+} luminous centers from shallow and deep traps. Thermally activated non-radiative energy transitions are reduced by such a phenomenon. Temperature clearly affects the self-trapped excitons' fluorescence intensity, when the temperature range is 20–260 °C. Contrarily, the fluorescence intensity of Mn^{2+} fluctuates slightly, making it an excellent candidate for use in materials for FIR temperature sensing. The results show that the probe has the best absolute sensitivity of 0.4443 K^{-1} at 533.15 K and the best relative sensitivity of 0.0142 K^{-1} at 453.15 K, indicating that the material has a good temperature measurement effect in the temperature range of 20–260 °C. This work provides a new type of temperature probe that is effective in high-temperature ranges and also shows the possibility of metal halide materials used in temperature measurement. Rb_4CdCl_6:Mn^{2+} single crystals were mixed with blue chips and released a bright white emission. These results will make it easier to investigate novel, highly PLQY Mn^{2+}-activated metal halides. Such metal halides can be used as a yellow component for display applications because they are thermally and chemically stable.

Conflicts of interest

There are no conflicts to declare.

Acknowledgements

This work is financially supported by the National Key Research and Development Program of China (2022YFB3503800) and the National Natural Science Foundation of China (NSFC No. 51932009, 61205113, 51902226, 52172166, U2005212), the Natural Science Fund of Heilongjiang Province (No. JJ2019LH0837), the 111 project (B13015) of Ministry Education of China to Harbin Engineering University, the Fundamental Research Funds for the Central Universities (No. 3072020CF2520), Project of High-level Scientific Research Guidance of Harbin Engineering University (No. 3072022TS2508), and the distinguished scientist fellowship program of King Saud University.

References

1 J. S. Manser, J. A. Christians and P. V. Kamat, Intriguing Optoelectronic Properties of Metal Halide Perovskites, *Chem. Rev.*, 2016, **116**(21), 12956–13008.

2 B. Saparov and D. B. Mitzi, Organic-Inorganic Perovskites: Structural Versatility for Functional Materials Design, *Chem. Rev.*, 2016, **116**(7), 4558–4596.
3 Y. Wei, Z. Y. Cheng and J. Lin, An overview on enhancing the stability of lead halide perovskite quantum dots and their applications in phosphor-converted LEDs, *Chem. Soc. Rev.*, 2019, **48**(1), 310–350.
4 L. N. Quan, B. P. Rand, R. H. Friend, S. G. Mhaisalkar, T.-W. Lee and E. H. Sargent, Perovskites for Next-Generation Optical Sources, *Chem. Rev.*, 2019, **119**(12), 7444–7477.
5 L. N. Quan, F. P. G. de Arquer, R. P. Sabatini and E. H. Sargent, Perovskites for Light Emission, *Adv. Mater.*, 2018, **30**(45), 1801996.
6 D. Magana, S. C. Perera, A. G. Harter, N. S. Dalal and G. F. Strouse, Switching-on superparamagnetism in Mn/CdSe quantum dots, *J. Am. Chem. Soc.*, 2006, **128**(9), 2931–2939.
7 D. J. Norris, N. Yao, F. T. Charnock and T. A. Kennedy, High-quality manganese-doped ZnSe nanocrystals, *Nano Lett.*, 2001, **1**(1), 3–7.
8 F. Locardi, M. Cirignano, D. Baranov, Z. Dang, M. Prato, F. Drago, M. Ferretti, V. Pinchetti, M. Fanciulli, S. Brovelli, L. De Trizio and L. Manna, Colloidal Synthesis of Double Perovskite $Cs_2AgInCl_6$ and Mn-Doped $Cs_2AgInCl_6$ Nanocrystals, *J. Am. Chem. Soc.*, 2018, **140**(40), 12989–12995.
9 W. Liu, Q. Lin, H. Li, K. Wu, I. Robel, J. M. Pietryga and V. I. Klimov, Mn^{2+}-Doped Lead Halide Perovskite Nanocrystals with Dual-Color Emission Controlled by Halide Content, *J. Am. Chem. Soc.*, 2016, **138**(45), 14954–14961.
10 B. B. Su, M. Molokeev and Z. G. Xia, Mn^{2+}-based narrow-band green-emitting Cs_3MnBr_5 phosphor and the performance optimization by Zn^{2+} alloying, *J. Mater. Chem. C*, 2019, **7**, 11220–11226.
11 V. Pinchetti, A. Anand, Q. A. Akkerman, D. Sciacca, M. Lorenzon, F. Meinardi, M. Fanciulli, L. Manna and S. Brovelli, Trap-Mediated Two-Step Sensitization of Manganese Dopants in Perovskite Nanocrystals, *ACS Energy Lett.*, 2019, **4**(1), 85–93.
12 B. Luo, Y. Guo, X. Li, Y. Xiao, X. Huang and J. Z. Zhang, Efficient Trap-Mediated Mn^{2+} Dopant Emission in Two Dimensional Single-Layered Perovskite $(CH_3CH_2NH_3)_{(2)}PbBr_4$, *J. Phys. Chem. C*, 2019, **123**(23), 14239–14245.
13 Q. Wei, M. Li, Z. Zhang, J. Guo, G. Xing, T. C. Sum and W. Huang, Efficient recycling of trapped energies for dual-emission in Mn-doped perovskite nanocrystals, *Nano Energy*, 2018, **51**, 704–710.
14 A. R. Zhang, J. C. Jin and Z. G. Xia, Tunable Luminescence of Sb^{3+} Doped 0D Cs_4PbCl_6 Nanocrystals from Three Distinct Emission Centers, *Adv. Opt. Mater.*, 2022, **10**, 2200720.
15 K. Han, J. W. Qiao, S. Zhang, B. B. Su, B. B. Lou, C. G. Ma and Z. G. Xia, Band Alignment Engineering in ns^2 Electrons Doped MetalHalide Perovskites, *Laser Photonics Rev.*, 2023, **17**, 2200458.
16 T. Hu, M. D. Smith, E. R. Dohner, M.-J. Sher, X. Wu, M. T. Trinh, A. Fisher, J. Corbett, X. Y. Zhu, H. I. Karunadasa and A. M. Lindenberg, Mechanism for Broadband White-Light Emission from Two-Dimensional (110) Hybrid Perovskites, *J. Phys. Chem. Lett.*, 2016, **7**(12), 2258–2263.
17 J. Jin, Y. Peng, Y. Xu, K. Han, A. Zhang, X.-B. Yang and Z. Xia, Bright Green Emission from Self-Trapped Excitons Triggered by Sb^{3+} Doping in Rb_4CdCl_6, *Chem. Mater.*, 2022, **34**(12), 5717–5725.
18 J. H. Han, N. S. M. Viswanath, Y. M. Park, H. B. Cho, S. W. Jang, J. W. Min and W. B. Im, Zero-Thermal-Quenching Layered Metal Halide Perovskite, *Chem. Mater.*, 2022, **34**(12), 5690–5697.
19 E. Hitzer, Crystal planes in Clifford geometric algebra, *Acta Crystallogr., Sect. A*, 2011, **67**, C333.
20 Z. Zhou, H. Zhu, X. Huang, Y. She, Y. Zhong, J. Wang, M. Liu, W. Li and M. Xia, Anti-thermal-quenching, color-tunable and ultra-narrow-band cyan green-emitting phosphor for w-LEDs with enhanced color rendering, *Chem. Eng. J.*, 2022, **433**.
21 Y. Gao, F. Huang, H. Lin, J. Zhou, J. Xu and Y. Wang, A Novel Optical Thermometry Strategy Based on Diverse Thermal Response from Two Intervalence Charge Transfer States, *Adv. Funct. Mater.*, 2016, **26**(18), 3139–3145.
22 M. Alencar, G. S. Maciel, C. B. de Araujo and A. Patra, Er^{3+}-doped $BaTiO_3$ nanocrystals for thermometry: Influence of nanoenvironment on the sensitivity of a fluorescence based temperature sensor, *Appl. Phys. Lett.*, 2004, **84**(23), 4753–4755.